

Mapping the surface potential, charge density and adhesion of cellulose nanocrystals using advanced scanning probe microscopy

Ankur Goswami^{a,b,*}, Kazi M. Alam^a, Pawan Kumar^a, Piyush Kar^a, Thomas Thundat^{c,d},
Karthik Shankar^{a,*}

^a Department of Electrical and Computer Engineering, University of Alberta, Edmonton, T6G 1H9, Canada

^b Department of Materials Science and Engineering, Indian Institute of Technology (IIT) Delhi, New Delhi, 11016, India

^c Department of Chemical and Materials Engineering, University of Alberta, Edmonton, T6G 1H9, Canada

^d Department of Chemical and Biological Engineering, University at Buffalo, The State University of New York, Buffalo, NY, 14260, USA



ARTICLE INFO

Keywords:

Cellulose nanocrystal

Surface charge

KPFM

EFM

Polysaccharides

Nanofibers

ABSTRACT

Cellulose nanocrystals (CNC) are the focus of significant attention in the broad area of sustainable technologies for possessing many desirable properties such as a large surface area, high strength and stiffness, outstanding colloidal stability, excellent biocompatibility and biodegradability, low weight and abundance in nature. Yet, a fundamental understanding of the micro- and nanoscale electrical charge distribution on nanocellulose still remains elusive. Here we present direct quantification and mapping of surface charges on CNCs at ambient condition using advanced surface probe microscopy techniques such as Kelvin probe force microscopy (KPFM), electrostatic force microscopy (EFM) and force-distance (F–D) curve measurements. We show by EFM measurements that the surface charge in the solid-state (as contrasted with liquid dispersions) present at ambient condition on CNCs provided by Innotech Alberta is intrinsically negative and the charge density is estimated to be $13 \mu\text{C}/\text{cm}^2$. These charges also result in CNCs having two times the adhesive force exhibited by SiO_2 substrates in adhesion mapping studies. The origin of negative surface charge is likely due to the formation of CNCs through sulfuric acid hydrolysis where sulfate half esters groups remained on the surface (Johnston et al., 2018).

1. Introduction

Products based on sustainable manufacturing processes and earth abundant renewable materials have become increasingly important in the last couple of decades due to concerns related to biodegradability, environmental pollution, and toxicity risks related to animal and human health. Cellulose is the most abundant biopolymer in the planet which is produced at a scale of 1.5×10^{12} tonnes per year (Klemm, Heublein, Fink, & Bohn, 2005). In its native form it has been used for thousands of years in cotton, wood, etc. which directly contributed to human civilization and cultures. On the other hand, there exist a wide variety of applications such as food additives, pharmaceuticals, paper production and construction, where cellulose and its derivatives have been used for more than a century (Habibi, Lucia, & Rojas, 2010; Ilyas, Sapuan, Sanyang, Ishak, & Zainudin, 2018; Mariano, El Kissi, & Dufresne, 2014; Osong, Norgren, & Engstrand, 2016; Zhang, Lin, & Yao, 2015). Therefore, the extraction and manufacture of forest-based products such as textiles, paper, wood and furniture constitutes a major

industry group in several major economies of the world (Brinchi, Cotana, Fortunati, & Kenny, 2013; Eichhorn, 2011).

Nanocelluloses (NCs) are semicrystalline polysaccharide fibers isolated from wood pulp, bagasse, hemp and other natural cellulose-rich sources by mechanical and chemical treatments (Capron, Rojas, & Bordes, 2017; Kargarzadeh et al., 2018; Sofla, Brown, Tsuzuki, & Rainey, 2016). These treatments include chemical hydrolysis, mechanical exfoliation and enzymatic approaches (Tan, Heo, Foo, Chew, & Yoo, 2019). Depending on the preparation methods a significant variation in the crystallinity, hydrophilicity, surface charge, elastic modulus and other physico-chemical properties are observed in the NCs, based on which they can be categorized in two groups. For instance, longer semi-crystalline fibrillar structures are called cellulose nanofibers (CNF) whereas the highly crystalline structures are called cellulose nanocrystals (CNCs). CNFs are flexible, micron-long nanofibers with widths of 5–20 nm whilst CNCs are 100–500 nm in length and 4–10 nm in diameter (Kafy et al., 2017).

A key potential application area for CNCs and CNFs involves their

* Corresponding author.

** Corresponding author at: Department of Electrical and Computer Engineering, University of Alberta, Edmonton, T6G 1H9, Canada.

E-mail addresses: agoswami@mse.iitd.ac.in (A. Goswami), kshankar@ualberta.ca (K. Shankar).

incorporation in reinforced polymeric composites and nanocomposites (Mariano et al., 2014; Miao & Hamad, 2013). CNCs are known to have a high strength (~ 7.6 GPa) as well as a high stiffness (~ 130 GPa) (Lee, Clancy, Konturi, Bismarck, & Shaffer, 2016), a combination of properties that makes them particularly desirable for use in polymer composites (Dufresne, 2013). While strength measures the total stress that can be borne by the material before failure, the stiffness is the slope of the stress-strain curve and measures the resistance of the material to elastic deformation. The surfaces of CNCs have been chemically modified by techniques such as polymer chain grafting, radical-mediated surface oxidation and surface esterification (Tang, Sisler, Grishkewich, & Tam, 2017). Both bare CNCs and surface-functionalized CNCs have been blended/cross-linked with a variety of hydrophilic and hydrophobic polymers including, but not limited to, poly(lactic acid), polyurethane, poly(ϵ -caprolactone), poly(vinylcetate), poly(vinylalcohol), polyethylene, poly(acrylic acid), polyacrylamide, poly(methylmethacrylate) and poly(acrylonitrile). Such CNC-polymer nanocomposites have been studied for use in light-weight, high strength biodegradable structural materials (Geng, Haque, & Oksman, 2016), adaptive mechanical and optical components (Fallon, Kolb, Herwig, Foster, & Bortner, 2019; Ko, Kim, Kim, Lee, & Kim, 2018), gas separation membranes (Jahan, Niazi, Hägg, & Gregersen, 2018), electrically conductive membranes (Alam et al., 2019; Xiong et al., 2016), proton exchange membranes (Ni et al., 2018), epoxy resins (Trinh & Mekonnen, 2018) and stimulus-responsive hydrogels (Kelly et al., 2013). All these applications demand the mixing of both bare and chemically modified CNCs with diverse solvents, polymers and other additives which in turn, depends on the interfacial interactions of CNCs. The interfacial properties of CNCs in blends depend on their surface charge density, state of aggregation, size distribution, etc. In a recent paper, Jakubek et al. (Jakubek et al., 2018) point out that there exist a number of characterization challenges related to CNCs that are not satisfactorily addressed by currently used techniques such as dynamic light scattering and electron microscopy. In this work, we use advanced scanning probe microscopic techniques such as electrostatic force microscopy (EFM) and scanning Kelvin probe microscopy (KPFM) to measure the surface charge and charge-redistribution of CNCs.

The colloidal stability of CNC-containing dispersions in solvents and polymer gels is significantly influenced by the high surface charge density of CNCs. The bulk properties of nanocellulose gels and suspensions, involving charges, were studied using several rheological measurements in the past (Li et al., 2015; Shafiei-Sabet, Hamad, & Hatzikiriakos, 2012). However, the surface charge measurement of CNCs remained elusive as most of the measurements are carried out using indirect techniques such as zeta potential measurements (Prathapan, Thapa, Garnier, & Tabor, 2016) and conductometric titration experiments (Beck, Méthot, & Bouchard, 2015). Zeta potential depends on the electrostatic potential measurement at the shear plane which separates the Gouy-Chapman and the Stern layers of the electrostatic double layer (EDL). Hence, this potential is a measurement of surface charge of the object screened by the tightly bound inner Stern layer of counterions (Hunter, 1981). On the other hand, conductometric titration depends on the replacement of ions resulting from a change in ionic conductivity (Mendham, Denney, Barnes, & Thomas, 2000). In both these techniques, the measured surface charge of the CNCs depends on the type of solvents used, ionic strength (in case of conductometric titration) and their interaction with the solvent. These techniques are less relevant when native surface charge in the solid-state is required. Moreover, the surface charge measured by the above-mentioned techniques is only an estimate of the gross charge of the system, and does not allow measurement and mapping of the surface charge of individual CNCs.

Recently EFM and KPFM were used by some of the co-authors of this work to estimate the native surface charge of asphaltene and clay (Gaikwad, Hande, Das, Mitra, & Thundat, 2015; Liu, Gaikwad, Hande, Das, & Thundat, 2015). Here we extend these techniques to estimate the

surface charge behavior of CNCs synthesized by Innotech Alberta, Canada. Our study had three specific objectives. First, to understand the surface potential of CNCs, which necessarily derives from the work function difference, static charge and applied bias of the system using the KPFM technique. Secondly, to quantify the amount of native charge present on the surface under ambient condition and map the intrinsic charges by measuring the frequency shift in EFM technique. Thirdly, to assess the type of charges prevalent on the surface by injecting additional charge and measuring the resulting frequency shift using the EFM technique.

2. Experimental section

2.1. Materials

Cellulose nanocrystals were supplied by Innotech Alberta (Edmonton, Canada). These CNCs were H_2SO_4 hydrolyzed and extracted from wood pulp. Elemental analysis using CHNS testing indicated that C, H and S content are 40.88, 6.11 and 1.17 wt.% respectively (Alam et al., 2019). There were, as expected, no measurable quantities of nitrogen. The XRD and Raman spectra of CNCs are shown in Figs. S1 and S2 respectively (see supporting information).

2.2. Sample preparation

CNC whiskers were obtained from Alberta Innovates in solid form. A clear non-turbid suspension of CNCs was prepared by dispersing the CNCs in deionized water using probe sonication for 2 h. Once the suspension was prepared, a 30 μL droplets from diluted and non-diluted suspensions were drop casted on a piranha cleaned 500 nm thick thermally grown silicon oxide wafer (SiO_2/Si) and also on a 50 nm Au coated silicon oxide wafer (SiO_2/Si). By baking the wafer at 100 $^\circ\text{C}$ on a hot plate for 3 h, the deposited CNC sample was dried and prepared for peak force KPFM and EFM measurements (Fig. 1). Thermally grown oxide wafer was used for EFM measurement whereas Au coated wafer was used for KPFM measurement. Both these wafers also dried at 100 $^\circ\text{C}$ on a hot plate for 3 h to remove surface water.

2.3. AFM, KPFM and EFM measurements

In order to carry out the AFM, KPFM and EFM measurements, the samples were grounded by connecting them to the AFM chuck holder using conductive copper tape. All the surface probe related

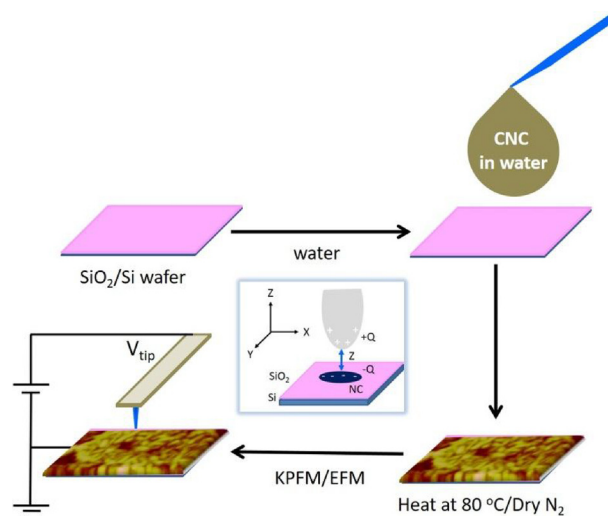


Fig. 1. Schematic illustration of sample preparation prior to scanning probe microscopy.

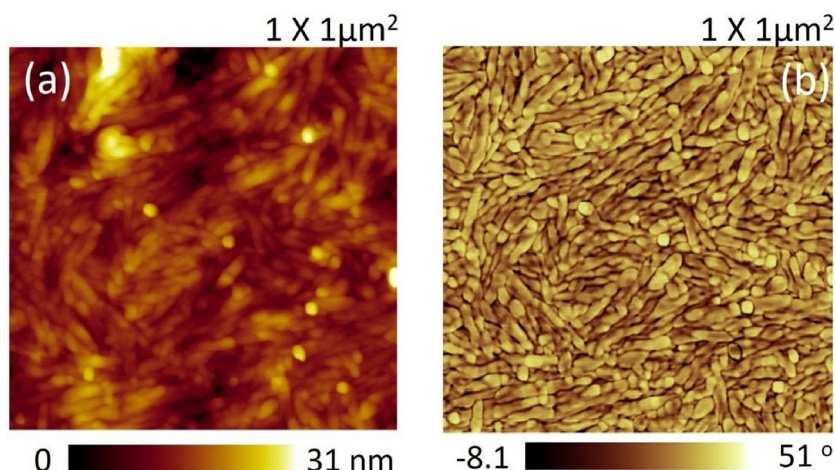


Fig. 2. (a) Topography of NC and its (b) corresponding phase images.

measurements were carried out using a Bruker Icon AFM system (Santa Barbara, CA). Electrically conducting SCN-PIT probes (App Nano, CA) with a resonance frequency of 73.8 kHz, quality factor of ~ 150 with a 30 nm diameter tip were used. There were four cantilevers used in the entire study and their spring constant were 4.1, 4.2, 4.7 and 4.8 N/m. In order to image the surface topography and phase response of the CNCs, tapping mode was adopted. Subsequently, peak force KPFM was conducted in order to image the surface potential of the CNCs. EFM was carried out to quantify the type and quantity of the native or fundamental charges on the surface. In order to measure the charges on the surface, EFM scan was performed at various lift heights of the probe which varied from 40 to 200 nm. Additionally, the tip bias was also varied from -5 to +5 V DC at an interval of 1 V at individual lift height. The analyses of the images were performed using Nanoscope analysis software (V1.40, Bruker). All the experiments were performed at room temperature (25 °C) and ambient atmosphere at 30–35 % humidity.

3. Results and discussion

The topographical and corresponding phase images of CNC aggregates are shown in Fig. 2a and b. From the height profile in Fig. 2a, the measured height of individual CNCs is of the order of 8–10 nm (see Fig. S3 in supporting information) whereas the roughness of the sample was found to be 3.5 nm (Foster et al., 2018). Parameters describing the average size of the CNC measured from different AFM images are found to be 143 ± 20 nm (length) and 18 ± 2 nm (cross section). The average aspect ratio of individual CNCs is found to be 8 which is seen to be lower than the literature (Reid, Villalobos, & Cranston, 2017).

The phase image of CNCs as shown in Fig. 2b clearly indicates the interwoven structure of CNC films which also depicts the variation of qualitative stiffness of the sample. This qualitative variation of stiffness across the phase image arises due to the variation in the semicrystalline nature of the sample. KPFM of CNCs was carried out in order to

measure the surface potential of the same. Fig. 3a and b show topography and the corresponding surface potential of a CNC layer on top of gold substrate. However, the scan area of these images ($20 \times 5 \mu\text{m}^2$) is significantly larger than the previous one ($1 \times 1 \mu\text{m}^2$). This allows one to visualize the clear contrast of surface potential of CNC and the gold substrate. The topography of the magnified region of Fig. 3a is shown in Fig. 3c, and its corresponding surface potential is shown in Fig. 3d. It is evident that the surface potential of the CNC is 100 mV negative w.r.t. the Au substrate.

In order to measure the surface charge distribution, EFM technique was adopted. In EFM measurement, two major signals are normally detected. One is surface topography during the trace and the other is change in frequency or phase of the AFM tip during retrace at a given constant lift height (z). The conductive AFM tip is sensitive enough to detect the charges on the surface by measuring the force gradient in the vertical direction *i.e.* $F'(z) \equiv \partial F/\partial z$. The force gradient is due to Coulombic forces $F(z)$ generated between the stored charges on the sample and its image charges on the tip. Therefore, the shift in frequency of the cantilever Δf with respect to the original resonance frequency f_0 can be expressed by the following equation at a specific lift height $z = z_0$.

$$\frac{\Delta f}{f_0} = -\frac{1}{2} \frac{\partial F/\partial z(z_0)}{k} \quad (1)$$

where $f_0 = 72$ kHz is the resonant frequency and $k = 4.2$ N/m is the stiffness of the cantilever used in this study.

Before performing EFM, a topographic image of one portion of CNC was chosen. The topographic image (Fig. 4a) indicates the chosen region to be comprised of a bunch of CNCs forming a layer. Fig. 4a and b show the topography of CNCs while Fig. 4c is the corresponding frequency map of the same taken from the yellow square region of Fig. 4a. The thickness of the CNC layer and corresponding frequency gradient is shown in Fig. 4d at 0 V tip bias and 50 nm lift height. Further scanning

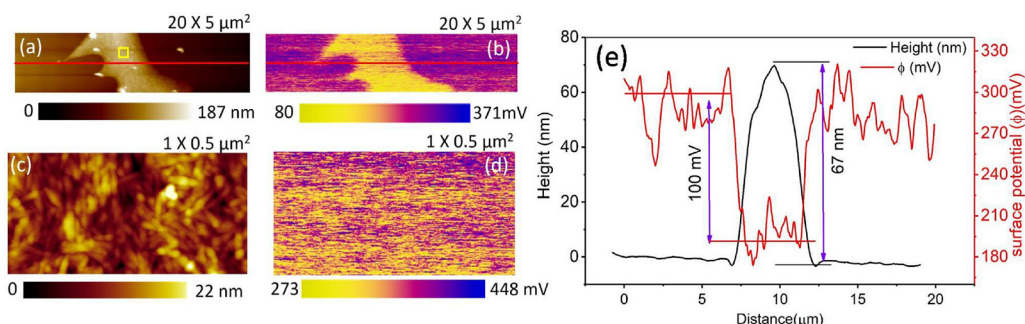


Fig. 3. (a) Topography and (b) corresponding surface potential measured from KPFM of CNC aggregates on Au coated SiO₂/Si wafer; (c), (d) are topography and surface potential of CNCs in the magnified yellow square region of image (a); (e) shows height and corresponding surface potential variation across the red marked line in images (a) and (b).

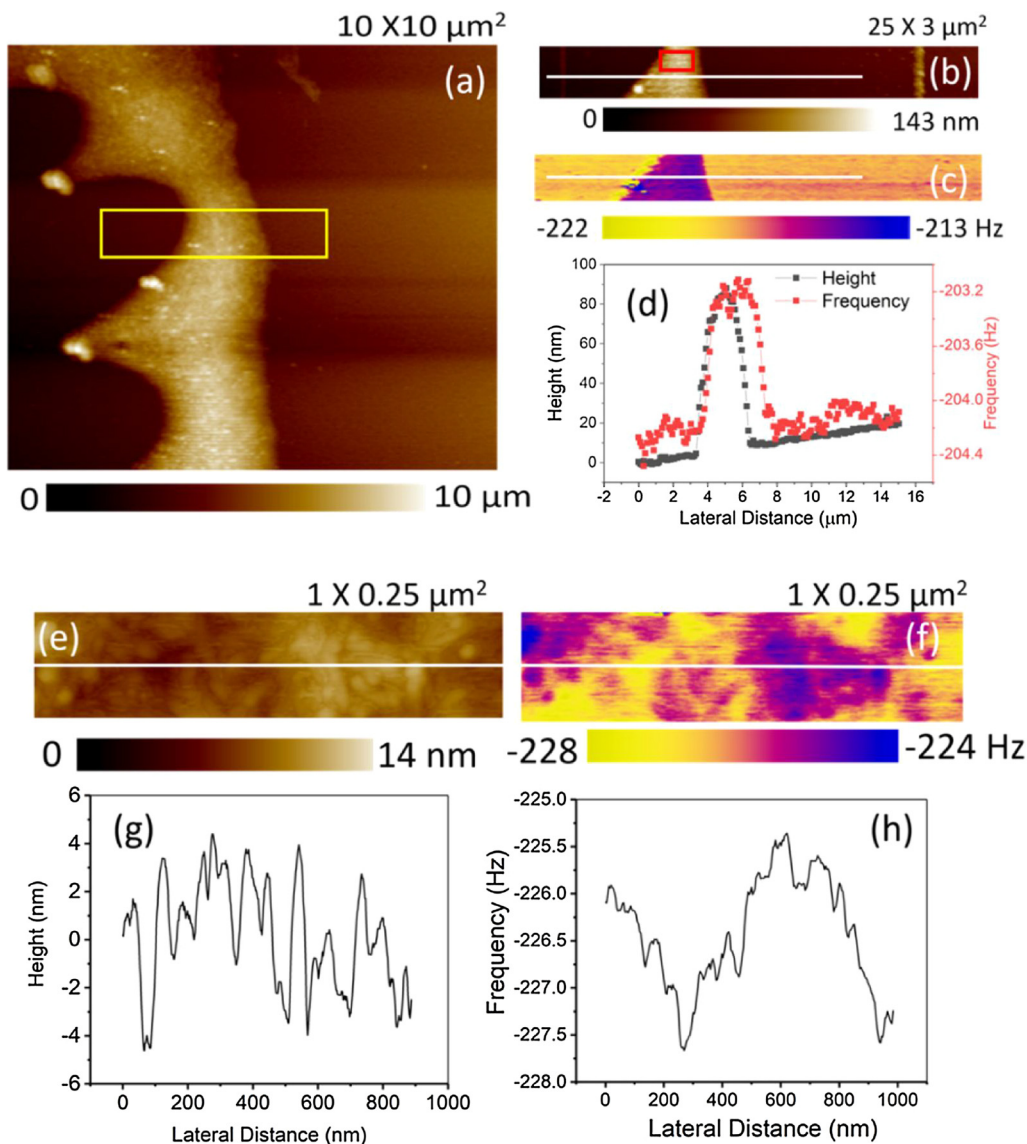


Fig. 4. (a) Topography of CNC sample (b) Shows the topography of the magnified square area and (c) corresponding frequency mapping at $V_{tip} = 0 V$ (d) Variation of height and frequency shift of the CNC sample as compared to the Si/SiO₂ wafer (e) shows the topography of the CNC sample taken from the magnified red square area of Fig. 4(b) and its corresponding frequency mapping in EFM scan (g) and (h) show the height and frequency variation inside the CNC sample through the marked white line.

the square area marked in red in Fig. 4b, the topography of individual CNCs can be seen which are entangled with each other (Fig. 4e). The corresponding frequency map in Fig. 4f depicts the variation in frequencies of the entangled CNCs due to the local variation of charges present on the surface. Fig. 4g and h show the height of individual CNCs and the fluctuation of frequencies respectively across the white line marked on Fig. 4e and f.

In order to measure the charge stored in the entangled CNC layer (Fig. 4b) we used a parallel plate capacitor model developed by Schaadt et al. (Schaadt, Yu, Sankar, & Berkowitz, 1999). By considering the CNC layer as a charged plate with a surface charge density of σ and using the above parallel plane capacitor model, the force $F(z)$ exerted on the cantilever due to the Coulombic interaction is given by the following expression

$$F(z) = \frac{A}{(z + t^*/\epsilon^*)^2} \times \left[-\frac{(t^*)^2\sigma^2}{2\epsilon_0(\epsilon^*)^2} + \frac{2t^*V_{tip}\sigma}{\epsilon^*} + \frac{\epsilon_0 V_{tip}^2}{2} \right] \quad (2)$$

where A is the surface area of the charged region, $t^* = t_{SiO_2} + t_{CNC}$ is the thickness of the capacitive layer, ϵ^* is the effective dielectric constant, z

is the tip-sample separation or in other words the lift height and V_{EFM} is the voltage applied to the tip during the EFM scan (tip bias). It is imperative from the first term of the parentheses that its contribution should be assuming no charge on the native minimal at $V_{tip} = 0$ and therefore, minimum contrast should be observed at zero tip bias provided surface charge is also nearly negligible. However, higher native surface charge would enhance the contrast at $V_{tip} = 0$ which we observe in Fig. 4c and f. The second term is more pronounced with higher V_{tip} and therefore the contrast of the image improves with higher tip bias. The last term is independent of the native or stored charge of CNCs which instead contributes to the background frequency shift of the whole frequency images of EFM measurement. By combining Eqs. (1) and (2), the following expression can be derived

$$\Delta f = \frac{f_0 A}{k(z + t^*/\epsilon^*)^3} \times \left[-\frac{(t^*)^2\sigma^2}{2\epsilon_0(\epsilon^*)^2} + \frac{2t^*V_{tip}\sigma}{\epsilon^*} + \frac{\epsilon_0 V_{tip}^2}{2} \right] \quad (3)$$

The EFM measurements were taken at the same location at +1 V tip bias by changing the lift height (z), as shown in the Fig. S4 (see supporting information). Fig. 5 shows the variation of Δf with the function

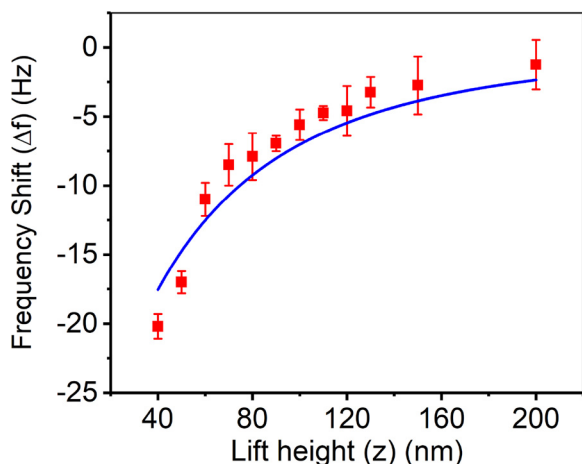


Fig. 5. Variation of frequency shift as a function of lift height. The blue curve shows the fitted plot as per Eq. (3) considering parallel plate EFM model.

of z and fitted to Eq. (3). The error bar indicates the variation of frequency has been taken from different parts of the plateau area. As expected from Eq. (3), Δf varies inversely with the lift height as the electrostatic force becomes weaker with increasing tip-sample distance. Considering $f_0 = 72$ kHz, $k = 4.2$ N/m, $A = 1.63 \times 10^{-13}$ m², $t^* = t_{\text{SiO}_2} + t_{\text{CNC}} = (500 + 67)$ nm, $\epsilon^* = 11.1$, $\epsilon_0 = 8.85 \times 10^{-12}$ and $V_{\text{tip}} = +1$ V, estimated charge density is obtained to be $13 \mu\text{C}/\text{cm}^2$ using Eq. (2). The regression coefficient is 0.91 implying a good fit of the analytical model equation to the experimental data of the surface charge using the existing theoretical model. The estimated charge from this model matches quite well with the charge measurement on CNC ($0.1\text{--}1$ e/nm²) performed by conductometric titration or zeta potential measurements as reported in literature (Reid et al., 2017; Vanderfleet, Osorio, & Cranston, 2018). Although the above model quantifies the native permanent charge on the CNC layer, it does not indicate the type of surface charge (positive or negative), on the sample. In order to find out the type of charge, the following experiments were performed. While conducting EFM experiments the major force that the cantilever can experience depends on the electrical field across which the cantilever is moving. Assuming no charge on the native substrate and on the particles spread on the substrate, the force gradient on the tip can be expressed as (Thierry Mélin, Zdrojek, & Brunel, 2010)

$$\frac{\partial F}{\partial z}(z_0) = \frac{1}{2} \frac{\partial^2 C}{\partial z^2} (V_{\text{tip}} - V_s)^2 \quad (4)$$

where $C(z)$ is the tip substrate capacitance and V_s represents the tip-substrate work function difference. Intuitively capacitive forces exerted on the cantilever lead to a frequency shift towards the negative end that varies as a square function of $(V_{\text{tip}} - V_s)$. However, after introducing or injecting Q charge from the tip to the substrate and on the CNC sample rested on the substrate, an effective built-in potential V_Q develops at the tip-substrate and tip-sample interfaces which results in the following effective force gradient.

$$\frac{\partial F}{\partial z}(z_0) = \frac{1}{2} \frac{\partial^2 C}{\partial z^2} [(V_{\text{tip}} - V_s)^2 - 2(V_{\text{tip}} - V_s)V_Q + V_Q^2] \quad (5)$$

From Eq. (5) it is discernible that because of the introduction of the charges, there are two additional components added as compared to Eq. (4) which contribute to the additional force gradient i.e. $(V_{\text{tip}} - V_s) \cdot V_Q$ and V_Q^2 . The first term i.e. $(V_{\text{tip}} - V_s) \cdot V_Q$ allows us to determine the sign of the native charges, as depending on the sign of V_Q (injected charge) the first term can alter its sign, and the second term i.e. V_Q^2 contributes to the image charge effect which always contribute to a larger negative frequency shift because of the attractive force gradient (Mélin, Diesinger, Deresmes, & Stiévenard, 2004; Mélin, Diesinger, Deresmes, & Stiévenard, 2004). However, the second term (V_Q^2) amplifies the EFM

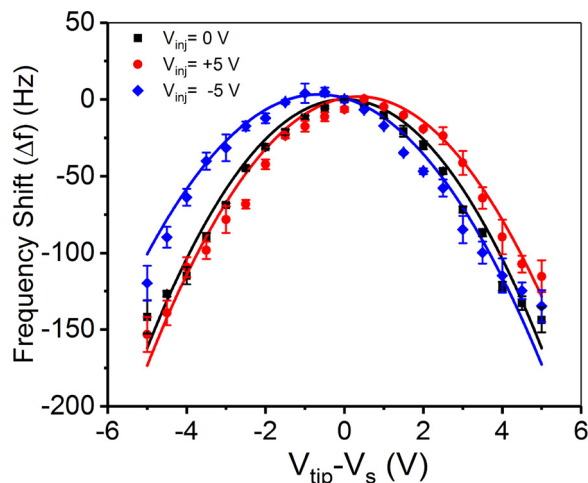


Fig. 6. Frequency shift in EFM experiment of CNC particle using various tip bias under lift mode by injecting no charge and +5 and -5 V charge.

frequency only while scanning over the dielectric layer but it is imperative that it is sign insensitive.

Considering Eqs. (4) and (5) above, the following EFM experiments were carried out and shown in Figs. S5–S7 (see supporting information). In the first case the EFM experiments were conducted on CNC layer on Si/SiO₂ substrate by varying tip bias from -5 V to +5 V at an interval of +1 V. This experiment results in a parabolic response of frequency shift with the function of tip bias as shown in Fig. 6 (black curve). After injecting positive ($V_{\text{inj}} = +5$ V) and negative charge ($V_{\text{inj}} = -5$ V) from the tip to the sample for 5 min by contact mode, the subsequent EFM experiments were conducted in lift mode. The subsequent EFM experiments at different bias were performed immediately after the charge injection and the whole experimental time scale was within 5 min in order to ensure that the dissipation of injected charges is not significant. It is observed from Fig. 6 that after injecting both types of charges the parabola becomes clearly asymmetric and is shifted either to the positive or negative side depending on the charge injection. However, due to negative charge injection the shifting of the parabola is more towards negative side and shows more asymmetry compared to the positive charge injection which confirms that the existing charges are negative (Mélin et al., 2004a).

The reason for this asymmetry is explained in the following discussion. Fig. 7(a)–(e) shows EFM images of CNC sample taken at different tip bias with and without charge injection. Fig. 7(f) shows the corresponding height of the CNC sample. It is observed from Fig. 7(g) that at zero tip bias when no charge is injected there is no change in frequency shift from the EFM data. However, at +5 V tip bias a large frequency shift is observed due to tip substrate capacitance response. As a result, over all baseline shift of the frequency (Δf_{i-s}) of 145 Hz is observed. However, while moving through the CNC sample the tip experiences additional capacitive force because of the native charge of the CNC sample which results in a further frequency shift (Δf_e) as shown in Fig. 7(h), the magnified part of Fig. 7(g). Subsequent to when charge is injected by setting tip bias to +5 V, the shift of frequency is not significant as compared to the case without charge injection. However, when charge is injected by setting tip bias to -5 V, a large frequency shift is observed. This explains that the CNC material possesses already negative native charge which gets more influenced when additional negative charge injection takes place. Therefore, when positive tip bias is used to measure EFM frequency, the existing negative charge become more pronounced because of the strong dipole formation. This results in more Coulombic attraction and thus shows a larger frequency shift.

In order to verify the presence of surface charges in the CNC samples, another indirect method was also adopted using adhesion mapping by employing quantitative nanomechanical analysis (QNM)

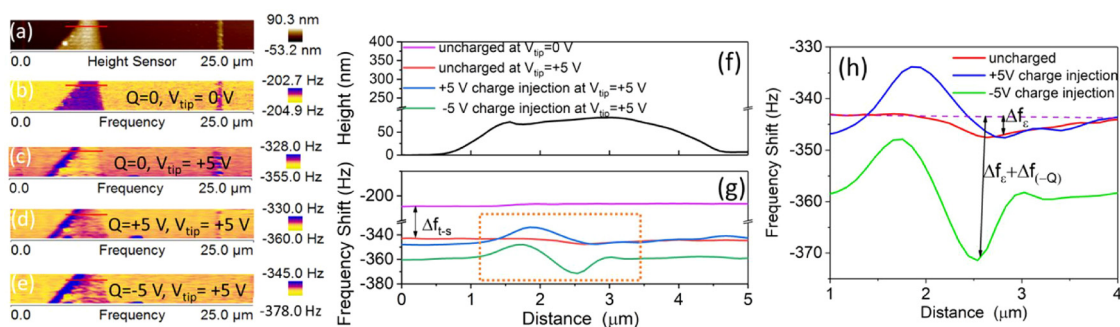


Fig. 7. (a)–(e) show EFM images of the CNC samples. (a) Topography of the CNC samples, EFM frequency images (b) at no charge injection ($Q = 0$ V) and $V_{tip} = 0$ V, (c) at $Q = 0$ V, $V_{tip} = +5$ V, (d) $Q = +5$ V, $V_{tip} = +5$ V, (e) $Q = -5$ V, $V_{tip} = +5$ V. (f) Height profile of the CNC samples, (g) frequency shift across the CNC sample at different condition. Applied $+5$ V tip bias shifts the base line frequency due to tip-sample capacitive force. (h) shows magnified image of square area of (g).

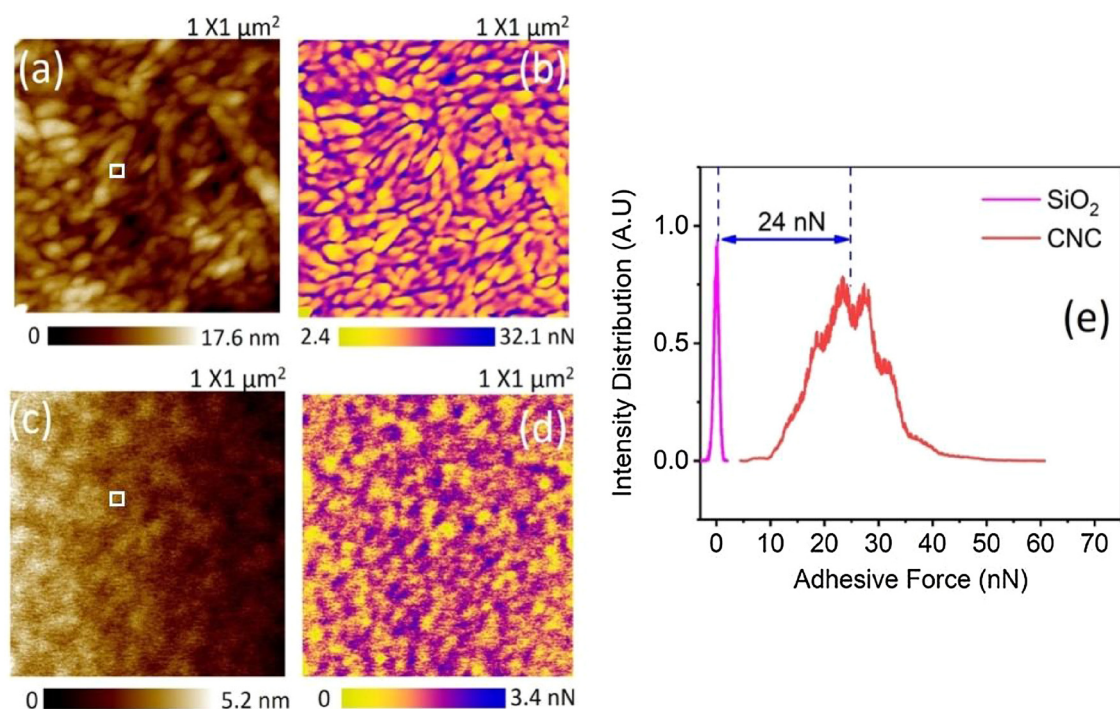


Fig. 8. (a) and (b) show the topography and adhesion mapping of CNC sample respectively. (c) and (d) depicts the topography and adhesion mapping of cleaned Si/SiO₂ wafer respectively. (e) show the comparative histogram of the entire adhesion map images of (b) and (d). The F-D curve measurement (shown in Fig. S8(a) and (b) (see supporting information)) were done on the small white square mark showed in image (a) and (c) for CNC and Si/SiO₂ respectively.

(Azzam et al., 2017; Smolyakov et al., 2017; Zhu, Soldatov, & Mathew, 2017). In addition, the force of adhesion is also measured using force-separation (F-D) curve in contact mode technique. Fig. 8(a) and (b) show the topography and corresponding adhesion mapping of the CNC samples while Fig. 8(c) and (d) show the piranha cleaned Si/SiO₂ wafer's topography and its corresponding adhesion map in order to compare two different systems. The adhesion maps clearly indicate that CNC samples possess a large distribution of the adhesive force as compared to Si/SiO₂ wafer which is likely due to the abundant surface charge on the former. From the histogram plot of the adhesive mapping of both SiO₂ and CNC surface (as shown in Fig. 8(e)) it is clear that CNC possesses much more adhesive force than SiO₂ which is mostly generated due to the charges present on the CNC surface. From the F-D curve data on CNC grains and on Si/SiO₂ wafer as shown in Fig. S8(a) and (b) respectively, it is observed that CNC sample has two times higher adhesive force than the Si/SiO₂ wafer which signifies the presence of charges that creates more pull-in force on the tip. It is important to note that in this case we believe the capillary forces exerted on the tip by both silicon and CNC surfaces are very minimal as the relative humidity was maintained at 30–35 % as mentioned before (Jones, Pollock,

Cleaver, & Hodges, 2002). Therefore, while measuring adhesive force, the major contribution is from the charges on the CNC surface. The negative charges originate from residual sulfate groups on the surface of CNCs obtained from Innotech Alberta that are synthesized through the hydrothermal sulfuric acid hydrolysis of wood pulp (Johnston et al., 2018).

4. Conclusions

Here we present mapping and estimation of native surface charge on CNC sample synthesized by acid hydrolysis method using KPFM and EFM method at ambient condition. Using a parallel plate model, we are able to estimate the native surface charge of CNC to be 13 $\mu\text{C}/\text{cm}^2$ in its solid-state form, whereas most of the reports till date are focused on charge measurement of CNC in liquid suspensions measured by zeta potential and conductometric titration. By injecting positive and negative charge into the CNC sample and measuring the EFM frequency shift with different tip bias we found that CNC sample is intrinsically negative charge which is due to the attachment of SO_4^{2-} counterions as sulfate half esters on to the sample. Our KPFM results show that the

surface potential of the sample is positive which indicates its work function is more than Pt/Ir tip and in the order of 5.15 eV ~ 5.25 eV. The adhesive mapping and F-z curve shows CNC possesses huge adhesive force at the surface which is twice the magnitude of clean Si/SiO₂ substrate due to the abundant of negative surface charge. This work showcases the power of advanced SPM techniques in performing non-contact characterization of the physicochemical properties of CNC-containing films. The native charge detection can provide better quantitative metrics for blends of CNC with polymers and other functional materials in the development of value added products based on CNCs.

CRedit authorship contribution statement

Ankur Goswami: Conceptualization, Methodology, Validation, Formal analysis, Investigation, Writing - original draft, Visualization. **Kazi M. Alam:** Investigation. **Pawan Kumar:** Formal analysis, Writing - review & editing, Visualization. **Piyush Kar:** Methodology, Formal analysis. **Thomas Thundat:** Resources. **Karthik Shankar:** Conceptualization, Visualization, Supervision, Project administration, Funding acquisition, Resources.

Acknowledgements

This work was made possible through direct and indirect funding support from NSERC, Alberta Innovates, FP Innovations, CMC Microsystems and NRC-NINT. The cellulose nanocrystal samples were provided by Innotech Alberta. We thank Dr. Wadood Hamad and his team at FP Innovations for constructive discussions. AG thanks Dr. Jun Liu from The State University of New York, Buffalo and Ms. Rosmi Abraham from CME, University of Alberta for helpful discussions on EFM data analysis.

Appendix A. Supplementary data

Supplementary material related to this article can be found, in the online version, at doi:<https://doi.org/10.1016/j.carbpol.2020.116393>.

References

- Alam, K. M., Kar, P., Thakur, U. K., Kisslinger, R., Mahdi, N., Mohammadpour, A., & Shankar, K. (2019). Remarkable self-organization and unusual conductivity behavior in cellulose nanocrystal-PEDOT: PSS nanocomposites. *Journal of Materials Science Materials in Electronics*, 30(2), 1390–1399.
- Azzam, F., Chaunier, L., Moreau, C., Lourdin, D., Bertoincini, P., & Cathala, B. (2017). Relationship between Young's Modulus and film architecture in cellulose nanofibril-based multilayered thin films. *Langmuir*, 33(17), 4138–4145.
- Beck, S., Méthot, M., & Bouchard, J. (2015). General procedure for determining cellulose nanocrystal sulfate half-ester content by conductometric titration. *Cellulose*, 22(1), 101–116.
- Brinchi, L., Cotana, F., Fortunati, E., & Kenny, J. (2013). Production of nanocrystalline cellulose from lignocellulosic biomass: Technology and applications. *Carbohydrate Polymers*, 94(1), 154–169.
- Capron, I., Rojas, O. J., & Bordes, R. (2017). Behavior of nanocelluloses at interfaces. *Current Opinion in Colloid & Interface Science*, 29, 83–95.
- Dufresne, A. (2013). Nanocellulose: A new ageless bionanomaterial. *Materials Today*, 16(6), 220–227.
- Eichhorn, S. J. (2011). Cellulose nanowhiskers: Promising materials for advanced applications. *Soft Matter*, 7(2), 303–315.
- Fallon, J. J., Kolb, B. Q., Herwig, C. J., Foster, E. J., & Bortner, M. J. (2019). Mechanically adaptive thermoplastic polyurethane/cellulose nanocrystal composites: Process-driven structure–property relationships. *Journal of Applied Polymer Science*, 136(4), 46992.
- Foster, E. J., Moon, R. J., Agarwal, U. P., Bortner, M. J., Bras, J., Camarero-Espinosa, S., ... Youngblood, J. (2018). Current characterization methods for cellulose nanomaterials. *Chemical Society Reviews*, 47(8), 2609–2679.
- Gaikwad, R., Hande, A., Das, S., Mitra, S. K., & Thundat, T. (2015). Determination of charge on asphaltene nanoaggregates in air using electrostatic force microscopy. *Langmuir*, 31(2), 679–684.
- Geng, S., Haque, M. M.-U., & Oksman, K. (2016). Crosslinked poly(vinyl acetate) (PVAc) reinforced with cellulose nanocrystals (CNC): Structure and mechanical properties. *Composites Science and Technology*, 126, 35–42.
- Habibi, Y., Lucia, L. A., & Rojas, O. J. (2010). Cellulose nanocrystals: Chemistry, self-assembly, and applications. *Chemical Reviews*, 110(6), 3479–3500.
- Hunter, R. J. (1981). Chapter 2 - Charge and potential distribution at interfaces. In R. J. Hunter (Ed.), *Zeta potential in colloid science* (pp. 11–58). Academic Press.
- Ilyas, R., Sapuan, S., Sanyang, M. L., Ishak, M. R., & Zainudin, E. (2018). Nanocrystalline cellulose as reinforcement for polymeric matrix nanocomposites and its potential applications: A review. *Current Analytical Chemistry*, 14(3), 203–225.
- Jahan, Z., Niazi, M. B. K., Hägg, M.-B., & Gregersen, Ø. W. (2018). Cellulose nanocrystal/PVA nanocomposite membranes for CO₂/CH₄ separation at high pressure. *Journal of Membrane Science*, 554, 275–281.
- Jakubek, Z. J., Chen, M., Couillard, M., Leng, T., Liu, L., Zou, S., & Johnston, L. J. (2018). Characterization challenges for a cellulose nanocrystal reference material: dispersion and particle size distributions. *Journal of Nanoparticle Research*, 20(4), 98.
- Johnston, L. J., Jakubek, Z. J., Beck, S., Araki, J., Cranston, E. D., Danumah, C., ... Mester, Z. (2018). Determination of sulfur and sulfate half-ester content in cellulose nanocrystals: An interlaboratory comparison. *Metrologia*, 55(6), 872.
- Jones, R., Pollock, H. M., Cleaver, J. A. S., & Hodges, C. S. (2002). Adhesion forces between glass and silicon surfaces in air studied by AFM: Effects of relative humidity, particle size, roughness, and surface treatment. *Langmuir*, 18(21), 8045–8055.
- Kafy, A., Kim, H. C., Zhai, L., Kim, J. W., Hai, L. V., Kang, T. J., ... Kim, J. (2017). Cellulose long fibers fabricated from cellulose nanofibers and its strong and tough characteristics. *Scientific Reports*, 7(1), 17683.
- Kargarzadeh, H., Mariano, M., Gopakumar, D., Ahmad, I., Thomas, S., ... Lin, N. (2018). Advances in cellulose nanomaterials. *Cellulose*, 25(4), 2151–2189.
- Kelly, J. A., Shukaliak, A. M., Cheung, C. C. Y., Shopsowitz, K. E., Hamad, W. Y., & MacLachlan, M. J. (2013). Responsive photonic hydrogels based on nanocrystalline cellulose. *Angewandte Chemie International Edition*, 52(34), 8912–8916.
- Klemm, D., Heublein, B., Fink, H. P., & Bohn, A. (2005). Cellulose: Fascinating biopolymer and sustainable raw material. *Angewandte Chemie International Edition*, 44(22), 3358–3393.
- Ko, H.-U., Kim, H. C., Kim, J. W., Lee, J., & Kim, J. (2018). Cellulose nanocrystal based transparent electroactive polyurethane for active lens application. SPIE.
- Lee, W. J., Clancy, A. J., Kontturi, E., Bismarck, A., & Shaffer, M. S. P. (2016). Strong and stiff: high-performance cellulose nanocrystal/poly(vinyl alcohol) composite fibers. *ACS Applied Materials & Interfaces*, 8(46), 31500–31504.
- Li, M.-C., Wu, Q., Song, K., Lee, S., Qing, Y., & Wu, Y. (2015). Cellulose nanoparticles: Structure–Morphology–Rheology relationships. *ACS Sustainable Chemistry & Engineering*, 3(5), 821–832.
- Liu, J., Gaikwad, R., Hande, A., Das, S., & Thundat, T. (2015). Mapping and quantifying surface charges on clay nanoparticles. *Langmuir*, 31(38), 10469–10476.
- Mariano, M., El Kissi, N., & Dufresne, A. (2014). Cellulose nanocrystals and related nanocomposites: Review of some properties and challenges. *Journal of Polymer Science Part B, Polymer Physics*, 52(12), 791–806.
- Mélin, T., Zdrojek, M., & Brunel, D. (2010). Electrostatic force microscopy and kelvin force microscopy as a probe of the electrostatic and electronic properties of carbon nanotubes. In B. Bhushan (Ed.), *Scanning probe microscopy in nanoscience and nanotechnology* (pp. 89–128). Berlin, Heidelberg: Springer Berlin Heidelberg.
- Mélin, T., Diesinger, H., Deresmes, D., & Stiévenard, D. (2004a). Electric force microscopy of individually charged nanoparticles on conductors: An analytical model for quantitative charge imaging. *Physical Review B, Condensed Matter*, 69(3), 035321.
- Mélin, T., Diesinger, H., Deresmes, D., & Stiévenard, D. (2004b). Probing nanoscale dipole-dipole interactions by electric force microscopy. *Physical Review Letters*, 92(16), 166101.
- Mendham, J., Denney, R. C., Barnes, J. D., & Thomas, K. (2000). *Vogel's textbook of quantitative chemical analysis*. England: Prentice Hall.
- Miao, C., & Hamad, W. Y. (2013). Cellulose reinforced polymer composites and nanocomposites: A critical review. *Cellulose*, 20(5), 2221–2262.
- Ni, C., Wei, Y., Zhao, Q., Liu, B., Sun, Z., Gu, Y., ... Hu, W. (2018). Novel proton exchange membranes based on structure-optimized poly(ether ether ketone)s and nanocrystalline cellulose. *Applied Surface Science*, 434, 163–175.
- Osong, S. H., Norgren, S., & Engstrand, P. (2016). Processing of wood-based microfibrillated cellulose and nanofibrillated cellulose, and applications relating to papermaking: A review. *Cellulose*, 23(1), 93–123.
- Prathapan, R., Thapa, R., Garnier, G., & Tabor, R. F. (2016). Modulating the zeta potential of cellulose nanocrystals using salts and surfactants. *Colloids Surface A: Colloids and Surfaces A*, 509, 11–18.
- Reid, M. S., Villalobos, M., & Cranston, E. D. (2017). Benchmarking cellulose nanocrystals: From the laboratory to industrial production. *Langmuir*, 33(7), 1583–1598.
- Schaadt, D. M., Yu, E. T., Sankar, S., & Berkowitz, A. E. (1999). Charge storage in Co nanoclusters embedded in SiO₂ by scanning force microscopy. *Applied Physics Letters*, 74(3), 472–474.
- Shafiei-Sabet, S., Hamad, W. Y., & Hatzikiriakos, S. G. (2012). Rheology of nanocrystalline cellulose aqueous suspensions. *Langmuir*, 28(49), 17124–17133.
- Smolyakov, G., Pruvost, S., Cardoso, L., Alonso, B., Belamie, E., & Duchet-Rumeau, J. (2017). PeakForce QNM AFM study of chitin-silica hybrid films. *Carbohydrate Polymers*, 166, 139–145.
- Sofla, M. R. K., Brown, R. J., Tsuzuki, T., & Rainey, T. J. (2016). A comparison of cellulose nanocrystals and cellulose nanofibres extracted from bagasse using acid and ball milling methods. *Advances in Natural Sciences: Nanoscience and Nanotechnology*, 7(3), 035004.
- Tan, K., Heo, S., Foo, M., Chew, I. M., & Yoo, C. (2019). An insight into nanocellulose as soft condensed matter: Challenge and future prospective toward environmental sustainability. *The Science of the Total Environment*, 650, 1309–1326.
- Tang, J., Sisler, J., Grishkewich, N., & Tam, K. C. (2017). Functionalization of cellulose nanocrystals for advanced applications. *Journal of Colloid and Interface Science*, 494, 397–409.
- Trinh, B. M., & Mekonnen, T. (2018). Hydrophobic esterification of cellulose nanocrystals

- for epoxy reinforcement. *Polymer*, 155, 64–74.
- Vanderfleet, O. M., Osorio, D. A., & Cranston, E. D. (2018). Optimization of cellulose nanocrystal length and surface charge density through phosphoric acid hydrolysis. *Philosophical Transactions Mathematical Physical and Engineering Sciences*, 376(2112), 20170041.
- Xiong, R., Hu, K., Grant, A., M, Ma, R., Xu, W., ... Tsukruk, V. V. (2016). Ultrarobust transparent cellulose nanocrystal-graphene membranes with high electrical conductivity. *Advanced Materials*, 28(7), 1501–1509.
- Zhang, Q., Lin, D., & Yao, S. (2015). Review on biomedical and bioengineering applications of cellulose sulfate. *Carbohydrate Polymers*, 132, 311–322.
- Zhu, C. T., Soldatov, A., & Mathew, A. P. (2017). Advanced microscopy and spectroscopy reveal the adsorption and clustering of Cu(II) onto TEMPO-oxidized cellulose nanofibers. *Nanoscale*, 9(22), 7419–7428.